Embedded Direct-Written Organic Micro-TEGs for High-Efficiency Skin-Heat Harvesting

Milad Jabri, Saeed Masoumi, Dimitrios Paparas, Mónica Acuautla, and Luigi Giuseppe Occhipinti**

Milad Jabri and Mónica Acuautla
Engineering and Technology institute Groningen, University of Groningen (RUG), Nijenborgh 4, 9747AG, Groningen, The Netherlands

CogniGron (Groningen Cognitive Systems and Materials Center), University of Groningen (RUG), Nijenborgh 3, 9747 AG Groningen, The Netherlands

Saeed Masoumi
Department of Mechanical, Manufacturing, and Biomedical Engineering, Trinity College Dublin, The University of Dublin, Dublin, Ireland
E-mail: smasoumi22@gmail.com

Dimitrios Paparas and Luigi Giuseppe Occhipinti
Department of Engineering, University of Cambridge, Cambridge, UK
E-mail: lgo23@cam.ac.uk

Funding:
L.G.O. acknowledges funding from the UK Engineering and Physical Research Council (EPSRC), grants no. EP/W024284/1 and EP/K03099X/1. D.P. is funded by the EPSRC Centre for Doctoral Training in Agri-Food Robotics (AgriFoRwArdS), grant no. EP/S023917/1.
MJ and MA would like to acknowledge the financial support of the CogniGron research center and the Ubbo Emmius Funds (Univ. of Groningen).

Keywords: Wearable Thermoelectric Generators, Direct-Written Structures, Thermal Efficiency, Skin-Heat Harvesting, Finite Element Analysis

Abstract

Flexible thermoelectric generators (TEGs) are transforming wearable electronics by harvesting body heat as a sustainable power source, offering an alternative to conventional energy systems. However, their performance is often constrained by low thermal-to-electrical conversion efficiency. This work presents a detailed numerical investigation, based on finite element analysis (FEA), to optimize direct-written organic micro-TEGs (μ-OTEGs) embedded in flexible substrates for enhanced skin-heat energy harvesting. Organic semiconductors, including p-type poly(3,4-ethylenedioxythiophene):poly(styrenesulfonate) (PEDOT:PSS) and n-type poly(benzodifurandione)/benzodipyrandione (PBFDO/BPDO), were selected for their tunable electrical and mechanical properties. Key design parameters were systematically refined to maximize power density and conversion efficiency. The embedded structure effectively minimizes interfacial heat loss, ensuring stable performance across various body locations and thermal conditions. Under optimized conditions, the embedded-leg μ-OTEG increases the temperature gradient (ΔT) from 3.58 °C to 10.4 °C, raises the open-circuit voltage (V_{OC}) from 10.41 mV to 18.4 mV, and boosts the output power from 0.83 μW to 2.56 μW. Remarkably, the proposed architecture achieves over a 250% enhancement in thermal efficiency compared with conventional wearable TEGs, attributed to the optimized embedded configuration. These findings highlight the potential of direct-written organic TEGs as scalable, self-powered platforms for next-generation wearable and biomedical devices.

1. Introduction

The field of wearable technology has advanced rapidly alongside the spread of personalized electronic devices such as smartwatches, healthcare monitoring platforms, artificial intelligence systems, and the Internet of Things (IoT) [1-9]. Increasing attention has been directed toward the development of flexible, self-powered electronic systems fabricated from eco-friendly materials and utilizing renewable energy sources, including solar and thermal energy. These devices are particularly appealing due to their ability to conform to complex three-dimensional (3D) surfaces and irregular geometries such as the contours of the human body while operating independently of conventional batteries [10-14]. Energy harvesting from the human body represents a promising approach to ensure a continuous and sustainable power supply for wearable electronics. Several energy conversion mechanisms have been explored for this purpose, such as triboelectric [15], piezoelectric [16], pyroelectric [17], and thermoelectric generator (TEG) technologies [18]. With ongoing progress in flexible and skin-integrated electronics, the integration of self-sustained energy systems capable of dynamically interfacing with the human body is becoming increasingly feasible. Among these, TEGs are particularly notable for their inherent ability to deliver continuous direct current (DC) power without the need for complex energy management circuits, while also offering long-term stability and maintenance-free operation.

TEGs can effectively harvest sustainable energy from the temperature gradient between a heat source such as the natural heat emitted by human skin and the surrounding environment, converting thermal energy into electrical power through the Seebeck effect [19,20]. Despite their high TE efficiency, conventional inorganic semiconductor materials with high TE performance, including Bi_2Te_3 and Sb_2Te_3, are costly to fabricate, rely on scarce and toxic elements, and possess intrinsic rigidity [21-25]. For wearable applications, key parameters such as low weight, material composition, thickness, softness, flexibility, and conformability are as critical as overall efficiency and cost-effectiveness. Consequently, while inorganic TE materials are widely studied for their superior performance [26], their brittleness, toxicity, scarcity, and high density significantly limit their integration into body-heat harvesting systems. In contrast, organic-based TEGs offer remarkable advantages, including high mechanical flexibility, lightweight nature, environmental compatibility, and excellent biocompatibility, making them highly suitable for skin-conformal and wearable applications [27]. Extensive research efforts have therefore focused on developing flexible organic TEGs to optimize energy extraction from human body heat [28-35].

Bi_2Te_3-based TEGs built on flexible substrates such as PDMS, PEN, and PI have emerged as promising candidates for wearable energy harvesting due to their tunable mechanical compliance and favorable TE properties, enabling design-driven device architectures for on-skin operation [36-40]. Early flexible modules retained bulk Bi_2Te_3/Sb_2Te_3legs while employing eutectic gallium-indium (EGaIn) liquid-metal interconnects, combining high TE performance with stretchable, skin-conformal packaging [41,42]. Optimization of filler thermal conductivity further improved ΔT across the TE legs and enhanced power density by balancing heat spreading and minimizing parasitic heat leakage [43]. A flexible TEG composed of p-type and n-type Bi_2Te_3 legs assembled on a PI substrate laminated with a copper electrode layer has been developed [44]. These TEG platforms, integrated with ultra-low-voltage energy management circuits and Bluetooth telemetry, enable stable sensing and wireless communication at temperature differences as small as 2-4 ℃, thereby minimizing the need for external batteries in wearable applications. Despite notable advancements, Bi_2Te_3-based flexible TEGs still face challenges related to material toxicity, and high density, which hinder their large-scale deployment in wearable technologies [45]. Their relatively heavy and voluminous structures contrast with the miniaturization trends of modern electronics and pose concerns for direct skin-contact applications due to the scarcity and potential toxicity of constituent elements. These limitations continue to drive the development of lighter, biocompatible, and miniaturized TE materials, as well as innovative packaging and thermal-architecture designs aimed at reducing mass and volume while maintaining milliwatt-level body-heat energy conversion [46].

Extensive research has explored conducting polymers such as polyaniline [47], polypyrrole [48], carbon-based composites [49], PEDOT:PSS [50] as promising flexible TE materials for organic-based TEGs. These materials are particularly attractive for next-generation wearable energy-harvesting systems due to their combination of mechanical flexibility and tunable TE performance, where electrical conductivity can be precisely tailored through chemical doping [51]. In this context, Massetti *et al.* [52] reported a fully direct-written organic μ-TEG based on printable p- and n-type TE inks, achieving monolithic integration on flexible substrates and demonstrating the feasibility of scalable, low-cost fabrication for self-powered microsystems. Organic-based flexible TEGs have found diverse practical applications, ranging from body-heat harvesting for wrist- and glove-integrated sensors to high-temperature monitoring and fire-warning systems, underscoring their versatility in self-powered wearable electronics. For example, flexible 3D spiral TEGs fabricated from PEDOT:PSS-tosylate/tellurium/single-walled carbon nanotube (PEDOT-Tos/Te/SWCNT) ternary nanocomposite films have achieved

output powers of 7.04 and 9.59 μW under an 80 °C temperature difference when integrated into wrist-worn devices [53]. In glove-based applications, highly elastic and flame-retardant TE aerogels composed of PEDOT:PSS/SWCNT composites have been employed for self-powered high-temperature sensing and fire warning, reaching output powers up to 400 μW under a 300 °C gradient. Similarly, Du *et al.* [54] demonstrated a reduced graphene oxide (rGO)/rPEDOT:PSS-based self-powered motion sensor capable of accurately recognizing multiple hand movements. Although the power output of such organic TEGs typically lies within the milliwatt-to-nanowatt range, their eco-friendliness, lightweight nature, ease of synthesis, and material abundance continue to motivate efforts toward performance enhancement through improved material engineering and architectural optimization. For instance, Lv *et al.* [55] proposed a 3D spring-like TEG (S-TEG) composed of dual elastomer layers and thermally insulating air gaps to efficiently exploit vertical temperature gradients. Thermal modeling confirmed enhanced interfacial heat transfer, reduced internal heat leakage, and improved ambient heat dissipation, yielding an output of 749.19 nW under a 30 °C temperature difference using only three pairs of SWCNT-based p–n couples.

In parallel, several numerical and theoretical studies have investigated strategies for optimizing heat-energy harvesting in self-powered wearable systems [56-66]. Tang *et al*. [67] employed finite element modeling to develop a multifactor design roadmap for wearable μ-TEGs, identifying optimal parameters such as packing density, leg geometry, and convective heat transfer coefficient, whereas Suárez *et al.* [68] proposed a quasi-3D computational model to evaluate both rigid and flexible module designs. More recently, flexible thin-film TEG architectures designed for on-skin applications have provided detailed structural and thermo-mechanical frameworks optimized for curved, low-profile surfaces [69]. Another study systematically examined the effect of TE leg geometry in thin-film TEGs, revealing that leg shape strongly influences electrical performance, power density, and device footprint in flexible configurations [70]. While these studies have substantially advanced the understanding of individual aspects ranging from material to device modelling, the integration of organic μ-TEG design with human skin remains underexplored, representing an important direction for future development in self-powered wearable electronics.

In this work, we unveil a numerical study of skin-heat energy harvesting through a μ-OTEG ingeniously embedded in flexible substrates. Leveraging FEM simulations, we optimize critical design parameters such as leg geometry, dimensions, asymmetry ratio, electrode thickness, and leg numbers to overcome the challenges of integrating TEGs onto the human body, unlocking efficient thermal-to-electrical conversion. Moreover, to enhance the thermal efficiency of the

optimized flexible TEGs for wearable applications, we employ a design where thermoelectric (TE) legs are embedded within the substrate, significantly boosting performance through reduced heat loss and improved energy harvesting.

2. Methods

2.1. Simulation of TE device properties

A three-dimensional steady-state FEM was developed using COMSOL Multiphysics to numerically study the electrical and thermal properties of TEG devices. The optimization model for a film TE leg is described in Supporting Information Figure S1. Post-treated PEDOT:PSS, poly(benzodifurandione)/benzodipyrandione (BPDO) PBFDO/BPDO, and silver were selected as the materials for p- and n-type TE leg, and electrode, respectively. The electrical and thermal characteristics of these materials are detailed in Supporting information Table S1. The PEDOT:PSS and PBFDO/BPDO legs were treated as effective isotropic media, using the experimentally reported in-plane parameters as direction-independent inputs [50, 71]. This approximation is justified because the study focuses on the relative comparison of device architectures under identical material properties.

The p-type TE leg material, consisting of H_2SO_4- and NaOH-treated PEDOT:PSS reported by Fan et al.,[50] demonstrates state-of-the-art performance with a power factor of 334 $\mu W\ m^{-1}\ K^{-2}$ among PEDOT:PSS-based systems and their treatments. Meanwhile, the n-type leg material, derived from poly(benzodifurandione) (PBFDO) optimized via benzodipyrandione (BPDO) isomeric incorporation as reported by Ji et al.,[71] exhibits exceptional n-type characteristics with a power factor of 142 $\mu W\ m^{-1}\ K^{-2}$. Accordingly, it can be inferred that a TEG designed and fabricated using the optimized structure and material parameters would enable maximum harvesting of thermal energy from human skin. For optimization purposes, the hot-side temperature of the TE device and TEG was fixed at 95 °C, since organic TE materials such as PEDOT:PSS tend to exhibit degraded performance at higher temperatures. Moreover, a higher hot-side temperature increases the temperature gradient across the TE leg, thereby enhancing the Seebeck voltage and facilitating a clearer evaluation of parameter dependencies during optimization. Although most wearable devices operate within lower temperature ranges, it remains important to consider potential applications under elevated-temperature environments, such as in fire-resistant garments. In contrast, when simulating skin-based thermal energy harvesting, the skin temperature, serving as

the heat source, was varied to represent typical values observed across different body regions under cold, ambient, and hot environmental conditions. The cold-side electrode of the TEG was modeled under forced convective heat flux boundary conditions. Additionally, the convective heat transfer coefficient (h) was set to 22 W m^{-2} K^{-1}, as determined in our previous work [69], where h was obtained by experimentally calibrating simulated and measured temperature differences across a fabricated TEG under varying hot-side temperatures.

2.2. Mathematical, thermal, and electrical modeling

A mathematical modeling and simulation framework was employed to evaluate the performance of TEGs. The analysis was carried out using FEM to solve the coupled equations governing heat transfer and electrical conduction, enabling detailed examination of the mechanisms that influence and enhance power generation. In thermodynamics, heat flux density describes the rate of thermal energy transfer from a region of higher temperature to one of lower temperature. This transfer occurs through three primary mechanisms including thermal conduction, thermal convection, and thermal radiation which together provide a comprehensive understanding of the modes of heat transfer in the system. The corresponding heat fluxes for each mechanism are expressed by Equations (1) to (3):

$$Q_{Conduction} = \frac{k.A.(T_{Hot} - T_{Cold})}{t} \quad (1)$$

$$Q_{Convection} = h.A.(T_{Hot} - T_{Cold}) \quad (2)$$

$$Q_{Radiation} = \sigma'.A.(T_{Hot}^4 - T_{Cold}^4) \quad (3)$$

Here, k denotes the thermal conductivity (W·m^{-1}·K^{-1}), A is the surface area (m^2), T_{Hot} and T_{Cold} represent the hot- and cold-side temperatures (K), t is the material thickness (m), h is the convective heat transfer coefficient (W·m^{-2}·K^{-1}), and σ' is the Stefan–Boltzmann constant (5.67×10^{-8} W·m^{-2}·K^{-4}). Because radiative heat transfer typically becomes significant only at high temperatures, it can be neglected in organic and wearable TEG systems. Consequently, the dominant heat transfer mechanisms in such devices are thermal conduction and convection .[71] The **current density** (J) within a TEG is governed by the combined effects of the electric field, voltage, and temperature gradient, and can be expressed as follows:

$$J = -\sigma(\nabla V + S.\nabla T) \quad (4)$$

$$\nabla J = 0 \quad (5)$$

where σ is the electrical conductivity ($S \cdot m^{-1}$), V is the electric potential (V), S is the Seebeck coefficient ($V \cdot K^{-1}$), and ∇T represents the temperature gradient ($K \cdot m^{-1}$). The heat flux and current density within a TEG are intrinsically coupled through the fundamental TE effects, and their thermodynamic relationships can be expressed as follows:

$$\nabla(k\nabla T) + \frac{J^2}{\sigma} - TJ.\left[\left(\frac{dS}{dT}\right)\nabla T + (\nabla S)_T\right] = 0 \quad (6)$$

The TEG generates an V_{OC} as a result of the temperature difference across its hot and cold junctions through the Seebeck effect. This open-circuit voltage, measured across the output terminals in the absence of an external load, represents the maximum potential difference that the TEG can produce under open-circuit conditions. The open-circuit voltage of the TEG can be expressed as a function of the Seebeck coefficient of the TE material, the number of TE pair leg, and the temperature difference across the device, as follows:

$$V_{OC} = N.S.\Delta T \quad (7)$$

where N is the number of p–n leg pairs, S is the Seebeck coefficient ($V \cdot K^{-1}$), and ΔT is the temperatures difference across the TEG (K), respectively. The electrical current generated by a TEG is influenced by several factors, including the temperature difference across the device, the intrinsic TE properties of the materials, and the resistance of the external load. The temperature gradient across the TEG induces a voltage through the Seebeck effect, which in turn drives an electrical current through the circuit. The magnitude of this current can be determined using Ohm's law, accounting for both the internal resistance of the TEG and the external load resistance, as follows:

$$I = \frac{V_{OC}}{R_{TEG}+R_{Load}} \quad (8)$$

where I is the output current (A), V_{OC} is the open-circuit voltage (V), R_{TEG} is the internal resistance of the TEG (Ω), and $R_{Load}$is the external load resistance (Ω).

The maximum output power is achieved when the external load resistance is equal to the internal resistance of the TEG, i.e.,

$$P_{max} = \frac{{V_{\mathrm{OC}}}^2}{4R_{\mathrm{TEG}}} \quad (10)$$

3. Results and Discussion

To maximize the TE power output and thermal efficiency of the proposed direct-written μ-OTEG, a systematic numerical optimization was performed using FEA. The material p-type PEDOT:PSS and n-type PBFDO/BPDO, while the structural and geometrical parameters were varied to identify the optimal configuration. The analysis sequentially investigated the influence of the substrate material, leg shape, TEG thickness, leg cross-sectional area, asymmetry ratio, electrode thickness, and the number of TE legs on the overall device performance. Each parameter was optimized based on its impact on the ΔT, V_{OC}, TEG resistance (R_{TEG}), and maximum output power (P_{Max}). This multivariable optimization approach revealed critical trade-offs between thermal insulation and electrical transport, establishing a precise balance required for achieving high thermal efficiency in flexible μ-OTEG. Notably, embedding the TE legs within the substrate substantially reduced interfacial heat losses and improved the effective thermal gradient, leading to a significant enhancement in both power density and thermal-to-electrical conversion efficiency compared to conventional planar TEG architectures.

3.1. Substrate Material and Shape of TE Leg

The thermal and mechanical characteristics of the substrate have a profound impact on the TE performance of μ-OTEGs, primarily by dictating the ΔT across the TE legs. To elucidate this effect, five representative substrate materials like polyimide (PI), polyethylene naphthalate (PEN), polyethylene terephthalate (PET), glass, and aerogel were analyzed under identical geometric and boundary conditions. **Figure 1(a,b)** depicts the variations in ΔT, V_{OC}, R_{TEG}, and P_{Max}. Among these materials, aerogel exhibited the largest ΔT of 1.49 °C, leading to the highest V_{OC} (0.132 mV) and P_{max} (817.26 pW). This superior performance is attributed to the ultralow thermal conductivity of aerogel, which effectively minimizes heat leakage through the substrate and maintains a high temperature gradient across the TE junctions. In contrast, glass and PI, possessing higher thermal conductivities, exhibited greater parasitic heat losses, resulting in lower ΔT and reduced output power. The R_{TEG} remained nearly constant (~5.3 Ω) across all substrates, confirming that the electrical resistance is predominantly determined by the TE legs rather than the substrate.

From a physical standpoint, the substrate functions as both a mechanical support and a thermal interface that mediates heat transfer between the TE legs and the environment. Therefore, an optimal substrate should offer minimal thermal conductivity while maintaining adequate

flexibility for skin-mounted applications. The results clearly demonstrate that aerogel provides the best compromise between thermal insulation and mechanical compliance, making it an ideal candidate for flexible μ-OTEGs. Its ability to confine heat within the device enhances thermal coupling at the hot junction, thereby improving both power density and conversion efficiency.

Building upon this optimized substrate, the effect of TE leg geometry was further investigated to elucidate its influence on heat transfer and charge transport within the μ-OTEG. As illustrated in **Figure 1(c-e)**, twelve different leg shapes including symmetric and asymmetric configurations such as cuboid, cylindrical, trapezoidal, hexagonal, and triangular cross-sections were analyzed. To ensure a controlled and meaningful comparison, the twelve TE-leg geometries in Figure 1 were grouped into symmetric and asymmetric configurations under identical material properties and leg height. For the symmetric shapes (E, J, K, L), the cross-sectional area was kept identical so that only the geometric profile influenced heat and charge transport. For the asymmetric shapes (A–D, F–I), one surface area was maintained constant across all legs, while the second surface was reduced by the same factor for all asymmetric geometries. The resulting smaller surface areas were verified to be identical across the asymmetric group, ensuring a consistent degree of asymmetry. In addition, for some asymmetric profiles, multiple orientations relative to the vertical heat-flow direction were examined to capture orientation-dependent effects. Consequently, the observed variations in ΔT, V_{OC}, R_{TEG}, and P_{Max} are dominated by geometry-driven heat-flow behavior rather than differences in effective contact area. The comparison focused on ΔT, V_{OC}, R_{TEG}, and P_{Max} to determine the most efficient design. The results indicate that the asymmetric cylindrical leg (F) achieved the highest ΔT (3.2 °C) and V_{OC} (0.279 mV), owing to its enhanced ability to concentrate and guide heat flow toward the cold junction. Conversely, the hexagonal prism (K) exhibited the lowest ΔT (1.66 °C) and V_{OC} (0.147 mV), primarily due to lateral heat dissipation caused by its wider contact area. In terms of power generation, the symmetric cuboid leg (E) delivered the highest P_{Max} (1013 pW) and the lowest R_{TEG} (5.3 Ω), indicating superior electrical conduction and minimal internal resistance.

This trade-off highlights the delicate balance between thermal and electrical transport in μ-OTEGs: asymmetric geometries strengthen the thermal gradient and voltage generation, while symmetric geometries favor charge conduction and power output [70]. Among all tested shapes, the symmetric cuboid was identified as the most promising configuration, achieving the best compromise between heat confinement and electrical efficiency. These findings underscore the crucial role of geometric design in optimizing the thermoelectric response of flexible μ-OTEGs for wearable and biomedical energy-harvesting systems.

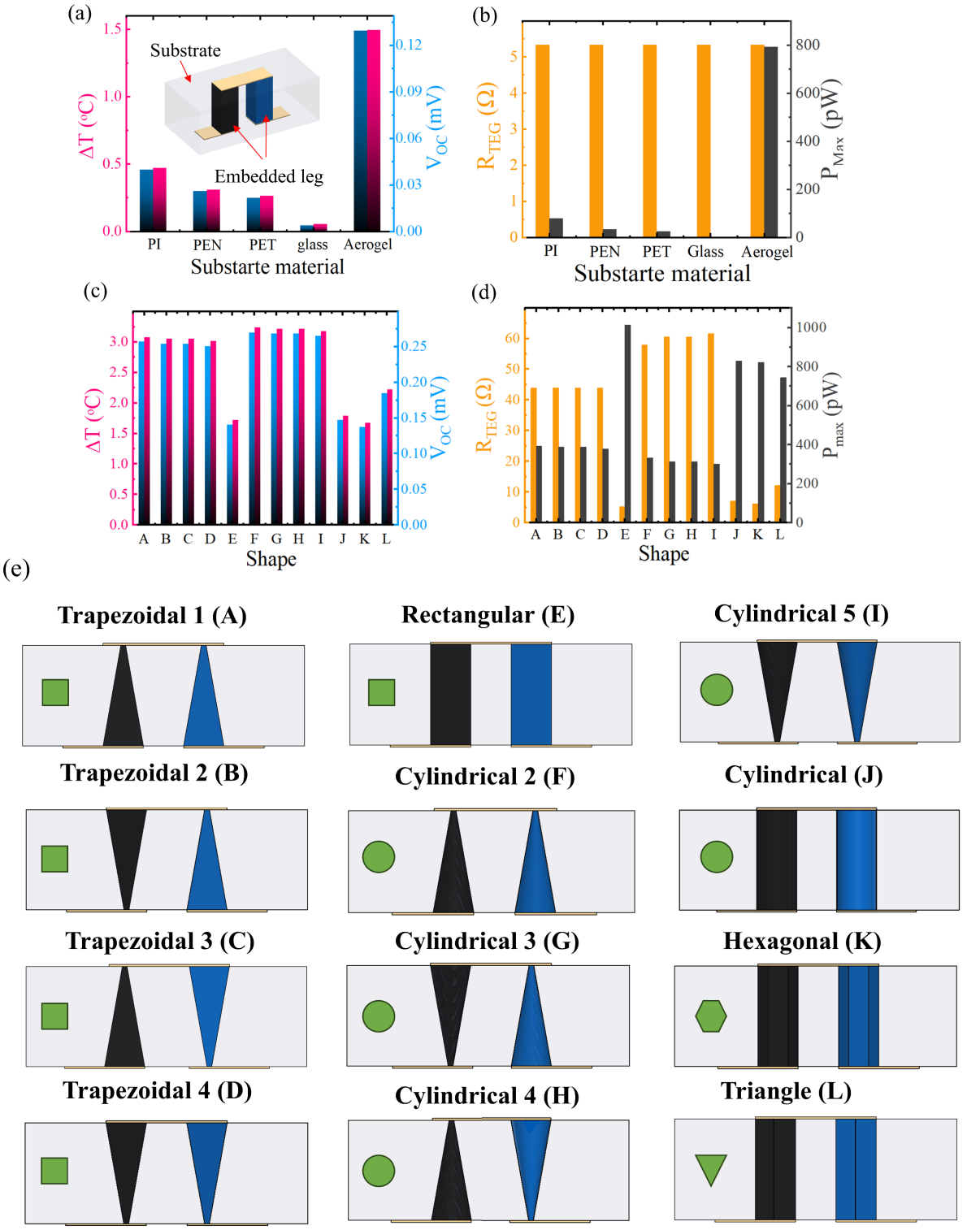

Figure 1. Effect of substrate material and leg geometry on the μ-OTEG performance. (a,b) ΔT, V_{OC}, R_{TEG}, and P_{Max} for different substrate materials (PI, PEN, PET, glass, and aerogel), (c,d) ΔT, V_{OC}, R_{TEG}, and Pmax for various leg geometries with both symmetric and asymmetric configurations, and (e) Schematic illustration of the investigated leg shapes (A–L), including cuboid, cylindrical, trapezoidal, hexagonal, and triangular cross-sections. Green icons indicate the cross-sectional shape of each TE leg.

3.2. TE Leg Optimization: TEG Thickness, Leg Area, and Asymmetry Ratio

Following the leg-shape analysis, the symmetric cuboid configuration identified as the most efficient geometry was adopted for further structural optimization. In the first stage, the TEG thickness was varied from 25 to 500 μm while maintaining a fixed leg width of 10 μm. **Figure 2(a-d)** shows the resulting variations in ΔT, V_{OC}, R_{TEG}, and P_{Max}. The output power initially increased with thickness, reaching a maximum P_{Max} of 68.2 nW at 300 μm. This behavior arises from the competing effects between thermal resistance and electrical path length: Increasing the TE-leg thickness enhances the effective thermal resistance along the vertical direction, allowing a larger temperature gradient to be sustained across the leg. Consequently, ΔT increases with thickness until reaching saturation, as shown in Figure 2(a). The optimal thickness thus represents the balance where sufficient heat flux and manageable internal resistance yield the highest overall power output. To evaluate the robustness of the identified optimum against material-property variations, we performed a sensitivity analysis by varying the Seebeck coefficient of the p-type (PEDOT:PSS) leg by ±30% while keeping other transport parameters unchanged, and re-optimizing the TE-leg thickness for maximum output power density. The results are provided in the Supplementary Information (Figure S3 and Table S2).

In the second stage, the TEG thickness was fixed at 300 μm, and the leg area was tuned by varying the square side length from 5 to 400 μm. **Figure 2(e-h)** illustrates the corresponding trends in ΔT, V_{OC}, R_{TEG}, and P_{Max}. The power output increased sharply with leg width due to enhanced electrical conduction and reduced internal resistance, reaching an optimal P_{Max} of 378.4 nW at 75 μm. In this study, the p-type and n-type legs were assigned identical widths to maintain a controlled geometry for architecture-level comparison and to ensure fabrication-compatible layouts in direct-written / thin-film μ-TEGs. Material-specific optimization of p/n leg dimensions (e.g., area ratio for resistance matching) is beyond the scope of the present work and may be explored in future studies. Further increases in leg width, however, promoted excessive heat spreading and decreased ΔT and V_{OC}, resulting in reduced performance. This outcome confirms that the leg area plays a key role in balancing heat confinement with efficient charge transport.

Finally, with both the TEG thickness and leg area fixed at their optimal values of 300 μm and 75 μm, respectively, the asymmetry ratio (A_2/A_1) of the leg was varied from 0.3 to 6, as shown in **Figure 2(i–l)**. The results reveal that a moderate asymmetry (ratio ≈ 0.9) delivers the maximum P_{Max} of 397.2 nW. In addition to P_{Max}, we report the optimized power density as a function of TEG thickness, square side length, and asymmetry ratio. The corresponding results are provided in the Supplementary Information (Figure S2). As shown in Figure S2, the

maximum power densities are 4.5, 25, and 26.2 mW/cm^2 for TEG thickness, square side length, and asymmetry ratio, respectively.

This improvement can be attributed to enhanced heat concentration near the hot junction and improved heat-flux directionality, which strengthen ΔT and V_{OC} without significantly affecting R_{TEG}. These findings demonstrate that a mildly asymmetric leg profile effectively optimizes the balance between thermal and electrical transport, maximizing the overall energy conversion efficiency of the μ-OTEG.

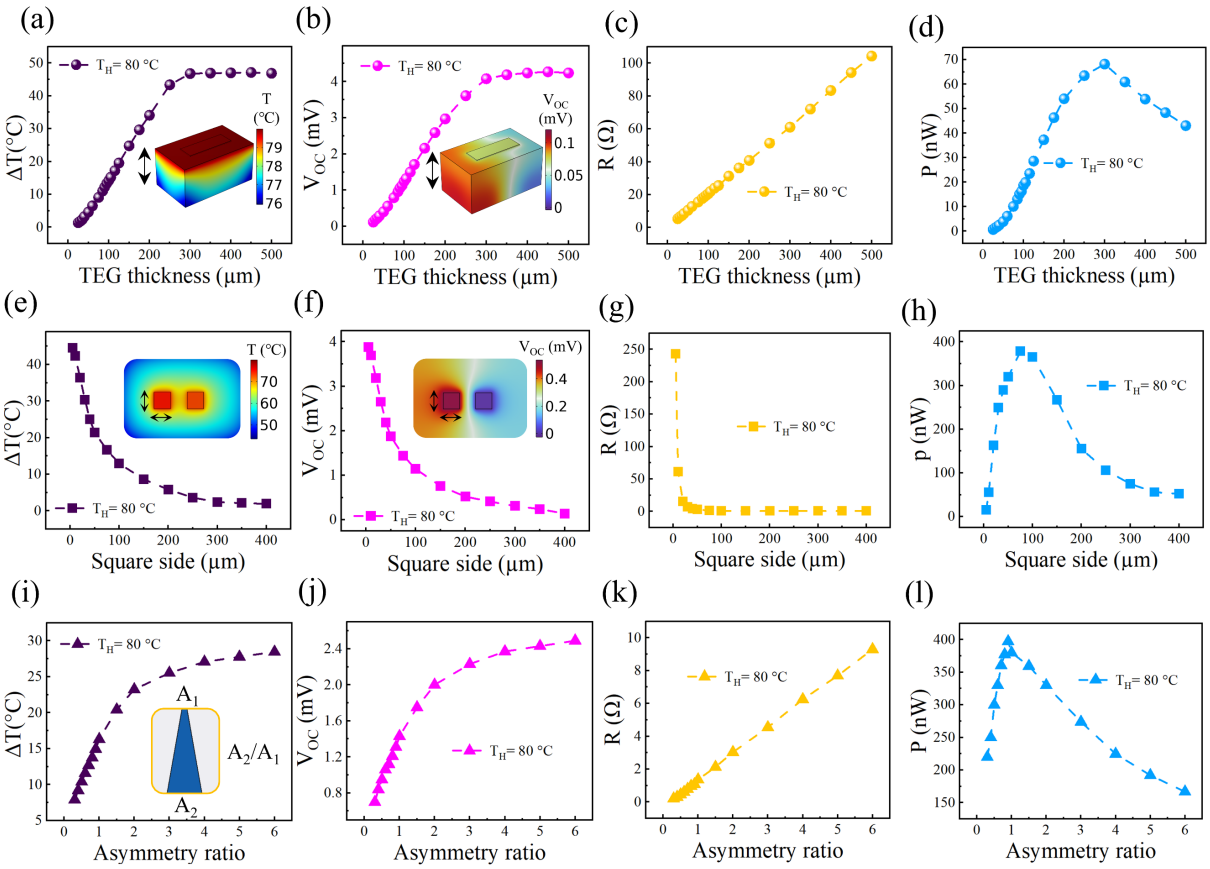

Figure 2. Optimization of the μ-OTEG structural parameters.
(a–d) Variations in ΔT, V_{OC}, R_{TEG}, and P_{Max} as a function of TEG thickness,
(e–h) Dependence of ΔT, V_{OC}, R_{TEG}, and P_{Max} on the leg area (square side length), and
(i–l) Effect of asymmetry ratio (A_2/A_1) on ΔT, V_{OC}, R_{TEG}, and P_{Max}.

3.3. Electrode thickness and leg numbers

The optimized μ-OTEG structure, comprising an asymmetric cuboid leg with a thickness of 300 μm, width of 75 μm, and asymmetry ratio of 0.9, was employed to investigate the influence of electrode thickness and leg number on device performance. The electrode thickness was first varied from 1 μm to 20 μm, and the resulting changes in ΔT, V_{OC}, R_{TEG}, and $P_{Max}$are shown in **Figure 3(a–d)**. As the electrode thickness increased, both ΔT and V_{OC} gradually rose due to improved interfacial heat spreading and reduced contact resistance, which enhanced the

effective temperature gradient across the thermoelectric legs. In contrast, R_{TEG} exhibited a rapid drop at small thicknesses (<5 μm) and then stabilized, indicating that further thickening no longer significantly impacts electrical conduction once a continuous low-resistance path is formed. Correspondingly, P_{Max} increased sharply with electrode thickness and reached saturation beyond 5 μm, where additional material contributed negligible improvements. This behavior reflects the dual thermal–electrical role of electrodes: thinner electrodes impede thermal coupling and increase Joule losses, while overly thick ones act as thermal sinks, causing lateral heat diffusion that reduces ΔT. Therefore, an intermediate electrode thickness of approximately 5 μm achieves the optimal trade-off between thermal conduction and electrical resistance, resulting in the highest Pmax of 498.36 nW.

In the final optimization stage, the number of TE legs was varied from 2 to 144 to examine its influence on overall module performance (**Figure 3(e–i)**). As the leg number increased, ΔT across individual legs decreased sharply and then stabilized beyond ~40 legs. This reduction originates from the formation of multiple parallel heat conduction paths: with more legs, the total cross-sectional area for thermal transport increases, enabling greater heat flow through the module and thereby lowering the temperature drop per leg. Simultaneously, V_{OC} increased almost linearly with leg number, consistent with the additive nature of the Seebeck effect, where each p–n couple contributes a fixed voltage increment. The R_{TEG} also rose proportionally due to longer cumulative current paths and additional contact interfaces. Despite this, P_{Max} continued to increase since the gain in V_{OC} outweighed the moderate rise in resistance, demonstrating that increasing leg number improves total output power up to a practical limit.

The thermal efficiency exhibited a nonmonotonic trend initially high for few-leg configurations and then decreasing and stabilizing at larger leg numbers. At small leg numbers, each leg experiences a larger ΔT, enabling stronger thermoelectric conversion efficiency. As leg numbers increases, however, the temperature difference per leg decreases because of enhanced heat spreading, leading to a reduction in the effective Carnot ratio ($\Delta T/T_{avg}$). Beyond a certain threshold (~40–60 legs), the efficiency approaches a steady value, indicating a quasi-equilibrium between electrical gain and thermal loss. This saturation reflects the intrinsic limitation of parallel thermal channels in μ-TEG arrays, where additional legs no longer contribute significantly to the net energy conversion due to thermal crowding and uniform temperature distribution across the base substrate. For instance, at 64 legs, the μ-OTEG achieved ΔT = 10.32 °C, V_{OC} = 32 mV, R_{TEG} = 32 Ω, P_{Max} = 2.7 μW, and a thermal efficiency of 0.07%, confirming its robust performance under realistic wearable conditions.

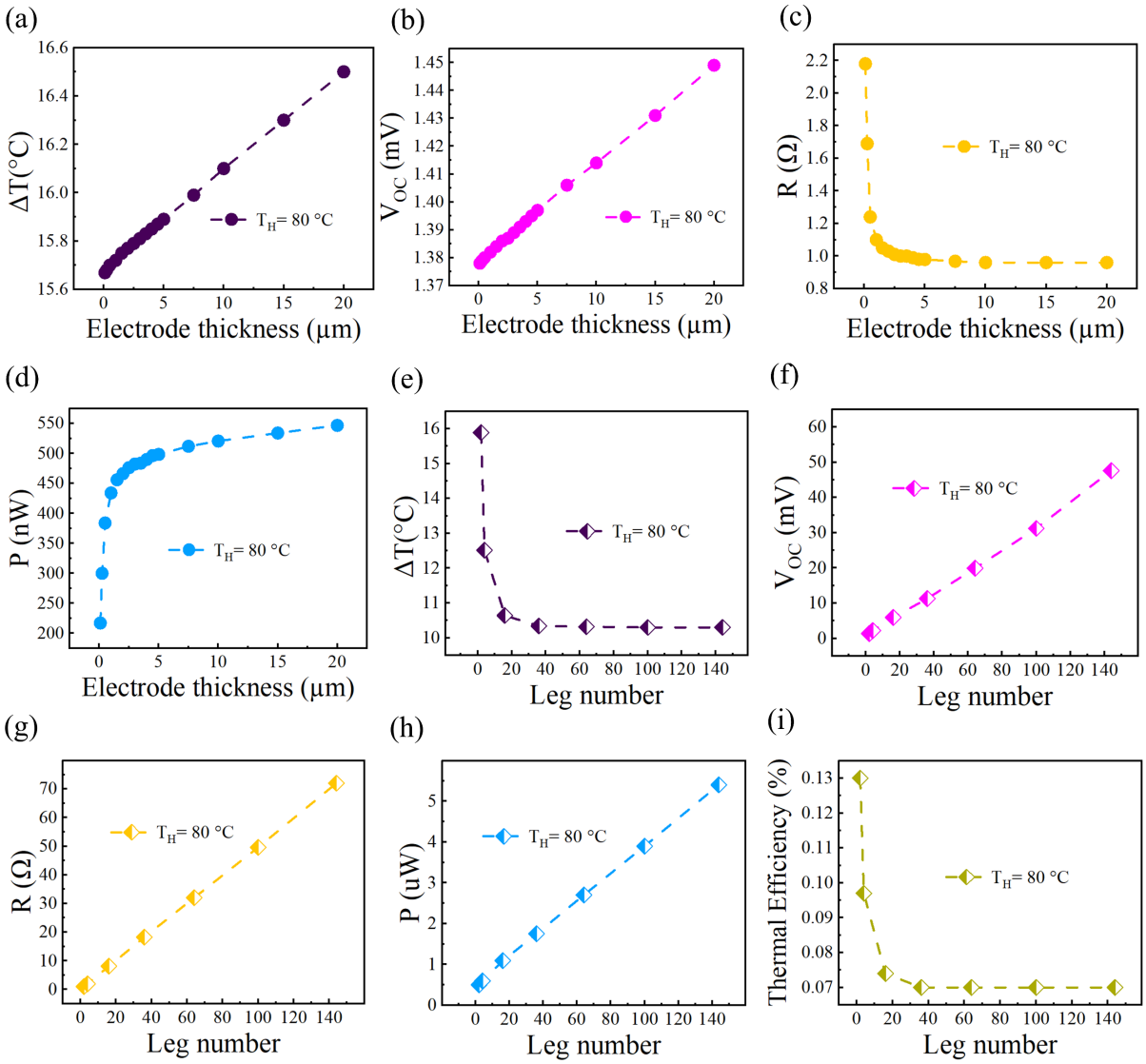

Figure 3. Effect of electrode thickness and leg number on μ-OTEG performance. (a–d) Variations in ΔT, V_{OC}, R_{TEG}, and P_{Max} as a function of electrode thickness and (e–i) Dependence of ΔT, V_{OC}, R_{TEG}, P_{Max}, and thermal efficiency on the number of thermoelectric legs.

3.4. Performance Comparison Between Embedded-Leg and Conventional TEGs

To highlight the effectiveness of the proposed embedded-leg configuration, the optimized μ-OTEG was compared with a conventional TEG of identical material composition and geometric footprint. Figures 4a and 4b present the steady-state temperature distributions of both architectures at a hot-side temperature of 80°C. In the conventional design, the TE legs are directly exposed on the substrate surface, leading to substantial lateral heat dissipation and poor confinement of the thermal gradient. As a result, the average ΔT across the TE legs was only 3.58 °C. In contrast, the embedded-leg configuration confines the TE elements within the low-conductivity substrate matrix, which effectively suppresses interfacial heat leakage and

concentrates the temperature drop across each leg. This design yields an enhanced ΔT of 10.4 °C approximately a threefold improvement confirming the superior heat management capability of the embedded structure.

Figure 4(c–f) compare ΔT, V_{OC}, P_{Max}, and thermal efficiency as functions of the hot-side temperature (T_{Hot}). Both ΔT and V_{OC} increase linearly with T_{Hot} for the two designs, yet the embedded-leg μ-OTEG consistently achieves higher values due to its improved vertical heat flow and reduced parasitic losses. The P_{Max} exhibits a quadratic-like dependence on T_{Hot}, reflecting the combined effect of voltage enhancement and decreased internal resistance at higher temperature gradients. Most notably, the embedded-leg configuration demonstrates a 295% increase in thermal efficiency compared with the conventional TEG, underscoring the critical role of geometric thermal confinement in maximizing energy conversion.

From a physical standpoint, embedding the TE legs within the substrate introduces an additional thermal barrier that redirects the heat flux vertically, minimizing lateral diffusion and maintaining a sharper temperature gradient across each junction. This confinement not only enhances the effective Seebeck voltage but also ensures a more uniform thermal distribution, leading to improved conversion efficiency and mechanical robustness under bending or skin contact. Consequently, the embedded-leg μ-OTEG architecture offers a scalable and energy-efficient platform for next-generation wearable thermoelectric energy harvesters.

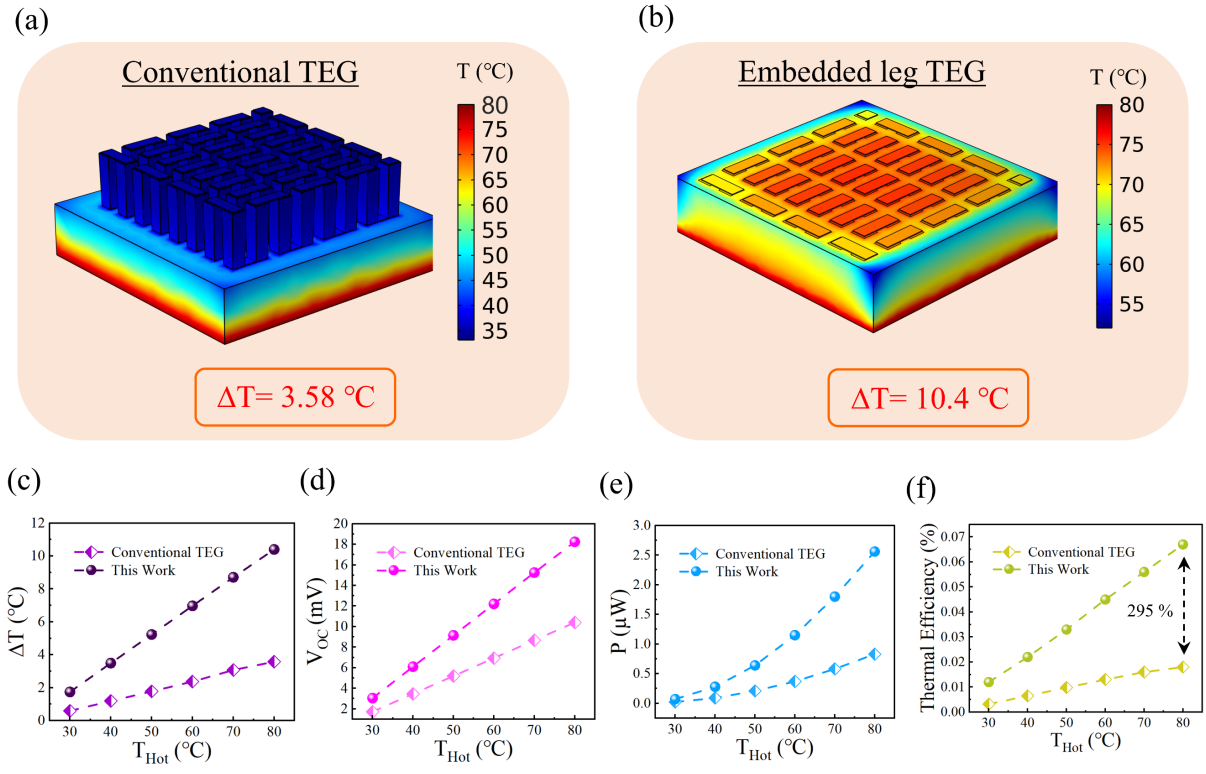

Figure 4. Comparison between conventional and embedded-leg μ-OTEG architectures. (a,b) Steady-state temperature distributions for conventional and embedded-leg configurations

at T_{Hot} = 80 °C and (c–f) Variations of ΔT, V_{OC}, P_{Max}, and thermal efficiency as functions of T_{Hot} for both designs.

3.5. Human skin-heat harvesting

TEGs have emerged as promising power sources for self-sustained electronics by exploiting the continuous heat flux from the human body. However, their practical performance is often limited by small temperature gradients between the skin and ambient air [69]. Numerous studies have attempted to enhance thermal-to-electrical conversion by improving material properties, optimizing heat exchangers, or integrating flexible substrates that conform to body contours [72-75]. Despite these efforts, maintaining a stable and sufficient ΔT across the TE legs under dynamic physiological conditions remains a key challenge. The proposed embedded-leg μ-OTEG design, which previously demonstrated a 295% improvement in thermal efficiency compared with conventional architectures, offers an ideal platform to assess real-world skin-heat energy harvesting. By embedding the thermoelectric elements within a thermally insulating substrate, interfacial losses are minimized, allowing efficient utilization of the natural temperature gradient across different body regions.

The optimized μ-OTEG, comprising 64 asymmetric cuboid legs (300 μm thickness, 75 μm width, asymmetry ratio of 0.9, and 5 μm electrode thickness), was evaluated on human skin at multiple anatomical sites under three ambient environments: cold (15 °C), room (27 °C), and hot (47 °C) (**Figure 5 (a-h)**). The corresponding skin temperatures for each location are summarized in **Table S3**. **Figures 5(i–l)** display the variations in ΔT, V_{OC}, P_{Max}, and thermal efficiency across the selected body locations. Among all sites, the head region (location D) exhibited the highest ΔT, V_{OC}, and P_{Max} across all thermal environments, reaching ΔT = 2.95 °C, V_{OC} = 5.17 mV, P_{Max} = 206.11 μW, and thermal efficiency = 0.019% under hot conditions. This superior performance can be attributed to enhanced local vascularization and proximity of major arteries to the skin surface, which result in higher and more stable skin temperatures . In contrast, peripheral regions such as the hand and foot showed smaller ΔT values due to weaker blood perfusion and more pronounced thermal regulation responses, especially under cold ambient conditions.

The observed dependence of performance on body location reflects the complex thermoregulation mechanism of human skin. Areas with greater metabolic activity, such as the head and neck, maintain higher steady-state heat flux and thus provide more favorable conditions for thermal energy harvesting [76]. The thermal efficiency of the μ-OTEG follows the same trend, increasing with ΔT and stabilizing at elevated ambient temperatures where the heat flux becomes approximately constant [77]. Overall, these results confirm that the

embedded-leg μ-OTEG can reliably harvest body heat with location-dependent performance, demonstrating significant potential for powering self-sustained wearable and biomedical electronics.

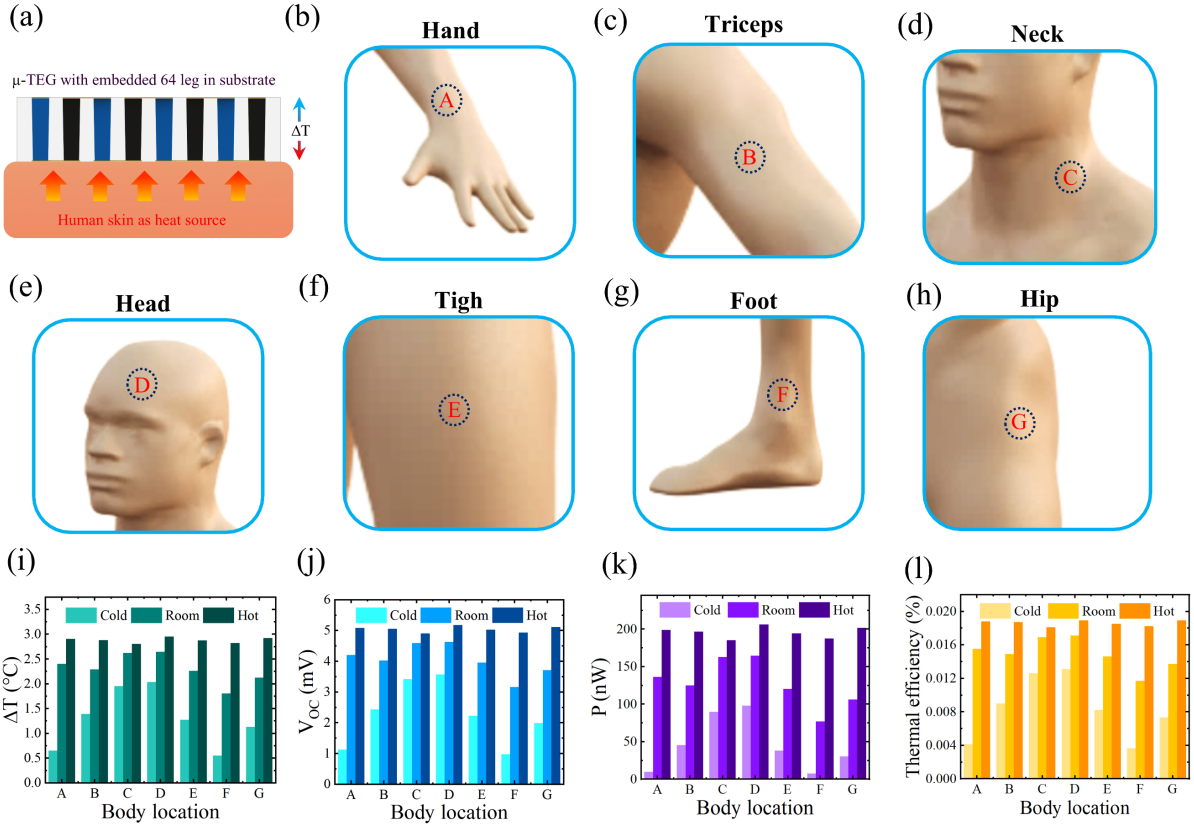

Figure 5. Evaluation of the optimized μ-OTEG for on-skin thermal energy harvesting. (a) Schematic of the embedded-leg μ-TEG structure attached to human skin as a heat source. (b–h) Selected body locations for performance assessment: hand (A), triceps (B), neck (C), head (D), thigh (E), foot (F), and hip (G) and (i–l) Variations in ΔT, V_{OC}, and P_{Max}, and thermal efficiency at different body locations under cold (15 °C), room (27 °C), and hot (47 °C) ambient conditions.

4. Conclusions

This study presented a comprehensive finite element–based optimization of a direct-written organic μ-OTEG designed for efficient harvesting of human body heat. Utilizing environmentally benign and mechanically compliant materials p-type PEDOT:PSS and n-type PBFDO/BPDO. The proposed architecture exploits the synergy between organic semiconductors and embedded thermal design to achieve high energy conversion performance. Systematic optimization of the key structural parameters, including substrate composition, leg geometry, TEG thickness, leg area, asymmetry ratio, electrode thickness, and leg number, revealed that the aerogel-supported μ-OTEG with asymmetric cuboid legs (300 μm thickness, 75 μm width, 0.9 asymmetry ratio), and 5 μm electrodes in a 64-leg configuration provides the

most favorable balance between thermal confinement and electrical conduction. Compared with conventional planar TEGs, the embedded-leg configuration achieved up to a 295% enhancement in thermal efficiency owing to its superior ability to suppress interfacial heat leakage and maintain a concentrated temperature gradient across the thermoelectric junctions. When evaluated under realistic human-skin conditions, the optimized μ-OTEG demonstrated stable, location-dependent performance across a wide range of ambient temperatures, with the head region exhibiting the highest ΔT, V_{OC}, and P_{Max} due to enhanced local vascularization and heat flux. These findings confirm the capability of the proposed μ-OTEG to reliably convert low-grade biological heat into electrical energy under practical wearable scenarios. Beyond demonstrating high performance, this work establishes a scalable and material-sustainable strategy for integrating organic thermoelectrics into flexible and skin-conformal platforms. The embedded-leg μ-OTEG architecture provides a robust blueprint for next-generation self-powered wearable and biomedical systems, bridging the gap between efficient thermal management, mechanical adaptability, and eco-friendly device engineering.

Acknowledgements

L.G.O. acknowledges funding from the UK Engineering and Physical Research Council (EPSRC), grants no. EP/W024284/1 and EP/K03099X/1. D.P. is funded by the EPSRC Centre for Doctoral Training in Agri-Food Robotics (AgriFoRwArdS), grant no. EP/S023917/1.

MJ and MA would like to acknowledge the financial support of the CogniGron research center and the Ubbo Emmius Funds (Univ. of Groningen).

Data Availability Statement

All data used in this study are included in the manuscript and supplementary information. Further data are available from the corresponding authors under reasonable request.

Supporting Information

Supporting Information is available from the Wiley Online Library or from the author.

References

[1] T.Q. Trung, N.E. Lee, Flexible and stretchable physical sensor integrated platforms for wearable human-activity monitoringand personal healthcare, Advanced materials 28 (2016) 4338–4372.
[2] J.C. Yang, J. Mun, S.Y. Kwon, S. Park, Z. Bao, S. Park, Electronic Skin: Recent Progress and Future Prospects for Skin-Attachable Devices for Health Monitoring, Robotics, and Prosthetics, Advanced Materials 31 (2019) 1904765.
[3] G. Lee, O. Hossain, S. Jamalzadegan, Y. Liu, H. Wang, A.C. Saville, T. Shymanovich, R. Paul, D. Rotenberg, A.E. Whitfield, Abaxial leaf surface-mounted multimodal wearable sensor for continuous plant physiology monitoring, Science Advances 9 (2023) eade2232.
[4] H. Choi, B.K. Min, S.J. Joo, B.S. Kim, K. Lee, H. Kang, Y.H. Sim, M.J. Yun, D.Y. Lee, S.I. Cha, Partially Air-Filled Skin-Attachable Deformable Gasket with Negative Poisson's Ratio for Highly-Efficient Stretchable Thermoelectric Generators, Advanced Energy Materials 13 (2023) 2301252.
[5] J. Ji, W. Zhao, Y. Wang, Q. Li, G. Wang, Templated laser-induced-graphene-based tactile sensors enable wearable health monitoring and texture recognition via deep neural network, ACS nano 17 (2023) 20153–20166.
[6] Y. Hao, J. Yang, Z. Niu, M. Wang, H. Liu, Y. Qin, C. Zhang, X. Li, High-output triboelectric nanogenerator based on L-cystine/nylon composite nanofiber for human bio-mechanical energy harvesting, Nano Energy 118 (2023) 108964.
[7] C. Tang, W. Yi, E. Occhipinti, Y. Dai, S. Gao, L.G. Occhipinti, A roadmap for the development of human body digital twins, Nature Reviews Electrical Engineering 1 (2024) 199–207.
[8] C. Tang, Z. Xu, E. Occhipinti, W. Yi, M. Xu, S. Kumar, G.S. Virk, S. Gao, L.G. Occhipinti, From brain to movement: Wearables-based motion intention prediction across the human nervous system, Nano Energy 115 (2023) 108712.
[9] M. Jabri, F. Hossein-Babaei, DC field-biased multibit/analog artificial synapse featuring an additional degree of freedom for performance tuning, Nanoscale 17 (2025) 3389–3401.
[10] M. Kang, R. Qu, X. Sun, Y. Yan, Z. Ma, H. Wang, K. Yan, W. Zhang, Y. Deng, Self-Powered Temperature Electronic Skin Based on Island-Bridge Structure and Bi-Te Micro-Thermoelectric Generator for Distributed Mini-Region Sensing, Advanced Materials 35 (2023) 2309629.
[11] S. Zhang, T. Bhatta, S.S. Rana, K. Shrestha, G.B. Pradhan, S. Sharma, S. Jeong, H.S. Kim, J.Y. Park, Noise-less hybrid nanogenerator based on flexible WPU and siloxene composite for self-powered portable and wearable electronics, Nano Energy 120 (2024) 109179.
[12] C. Bai, Z. Wang, S. Yang, X. Cui, X. Li, Y. Yin, M. Zhang, T. Wang, S. Sang, W. Zhang, Wearable electronics based on the gel thermogalvanic electrolyte for self-powered human health monitoring, ACS Applied Materials & Interfaces 13 (2021) 37316–37322.
[13] C. Wang, Z. Xu, H. Wang, T. Cai, H. Tao, Y. Wang, X. Tang, Combined energy supply and management of self-powered wireless sensors based on radioisotope thermoelectric generator for multiple scenarios, Energy Conversion and Management 297 (2023) 117706.
[14] Y. Jia, Q. Jiang, H. Sun, P. Liu, D. Hu, Y. Pei, W. Liu, X. Crispin, S. Fabiano, Y. Ma, Wearable thermoelectric materials and devices for self-powered electronic systems, Advanced Materials 33 (2021) 2102990.
[15] X. Pu, M. Liu, X. Chen, J. Sun, C. Du, Y. Zhang, J. Zhai, W. Hu, Z.L. Wang, Ultrastretchable, transparent triboelectric nanogenerator as electronic skin for biomechanical energy harvesting and tactile sensing, Science advances 3 (2017) e1700015.
[16] K. Shi, H. Xiao, S. Taleb, F.J. Flores-Ruiz, M. Acuautla, High-Performance of Piezoelectric and Ferroelectric PVDF-TrFE Based Composites Engineered by MWCNTs@ BaTiO3 Heterostructure, Small 21 (2025) e08878.

[17] H. Xue, Q. Yang, D. Wang, W. Luo, W. Wang, M. Lin, D. Liang, Q. Luo, A wearable pyroelectric nanogenerator and self-powered breathing sensor, Nano Energy 38 (2017) 147–154.
[18] S.J. Kim, J.H. We, B.J. Cho, A wearable thermoelectric generator fabricated on a glass fabric, Energy & Environmental Science 7 (2014) 1959–1965.
[19] G.J. Snyder, E.S. Toberer, Complex thermoelectric materials, Nature materials 7 (2008) 105–114.
[20] M. Jabri, S. Masoumi, F. Sajadirad, R.P. West, A. Pakdel, Thermoelectric energy conversion in buildings, Materials Today Energy 32 (2023) 101257.
[21] R. Venkatasubramanian, E. Siivola, T. Colpitts, B. O'quinn, Thin-film thermoelectric devices with high room-temperature figures of merit, nature 413 (2001) 597–602.
[22] H.-L. Zhuang, H. Hu, J. Pei, B. Su, J.-W. Li, Y. Jiang, Z. Han, J.-F. Li, High ZT in p-type thermoelectric (Bi, Sb) 2 Te 3 with built-in nanopores, Energy & Environmental Science 15 (2022) 2039–2048.
[23] B. Hinterleitner, I. Knapp, M. Poneder, Y. Shi, H. Müller, G. Eguchi, C. Eisenmenger-Sittner, M. Stöger-Pollach, Y. Kakefuda, N. Kawamoto, Thermoelectric performance of a metastable thin-film Heusler alloy, Nature 576 (2019) 85–90.
[24] L.-D. Zhao, S.-H. Lo, Y. Zhang, H. Sun, G. Tan, C. Uher, C. Wolverton, V.P. Dravid, M.G. Kanatzidis, Ultralow thermal conductivity and high thermoelectric figure of merit in SnSe crystals, nature 508 (2014) 373–377.
[25] F. Hossein-Babaei, S. Masoumi, A. Noori, Linking thermoelectric generation in polycrystalline semiconductors to grain boundary effects sets a platform for novel Seebeck effect-based sensors, Journal of Materials Chemistry A 6 (2018) 10370–10378.
[26] D. Cheikh, B.E. Hogan, T. Vo, P. Von Allmen, K. Lee, D.M. Smiadak, A. Zevalkink, B.S. Dunn, J.-P. Fleurial, S.K. Bux, Praseodymium telluride: a high-temperature, high-ZT thermoelectric material, Joule 2 (2018) 698–709.
[27] O. Bubnova, X. Crispin, Towards polymer-based organic thermoelectric generators, Energy & Environmental Science 5 (2012) 9345–9362.
[28] C. Wan, X. Gu, F. Dang, T. Itoh, Y. Wang, H. Sasaki, M. Kondo, K. Koga, K. Yabuki, G.J. Snyder, Flexible n-type thermoelectric materials by organic intercalation of layered transition metal dichalcogenide TiS 2, Nature materials 14 (2015) 622–627.
[29] M. Du, J. Ouyang, K. Zhang, Flexible Bi 2 Te 3/PEDOT nanowire sandwich-like films towards high-performance wearable cross-plane thermoelectric generator and temperature sensor array, Journal of Materials Chemistry A 11 (2023) 16039–16048.
[30] S. Hou, J. Huang, Y. Liu, Y. Luo, X. Wang, L. Yin, X. Sun, Z. Wu, J. Wang, J. Sui, Encapsulated Ag2Se-based flexible thermoelectric generator with remarkable performance, Materials Today Physics 38 (2023) 101276.
[31] D. Yang, D. Zhang, D. Ao, M. Nisar, A. Mansoor, Y. Chen, F. Li, H. Ma, G. Liang, X. Zhang, High thermoelectric performance of aluminum-doped cuprous selenide thin films with exceptional flexibility for wearable applications, Nano Energy 117 (2023) 108930.
[32] K.-C. Wang, P.-S. Lin, Y.-C. Lin, S.-H. Tung, W.-C. Chen, C.-L. Liu, Tunable Thermoelectric Performance of the Nanocomposites Formed by Diketopyrrolopyrrole/Isoindigo-Based Donor–Acceptor Random Conjugated Copolymers and Carbon Nanotubes, ACS Applied Materials & Interfaces 15 (2023) 56116–56126.
[33] S. Das, B.P. Mondal, P. Ranjan, A. Datta, High-performance paper-based thermoelectric generator from Cu2SnS3 nanocubes and bulk-traced bismuth, ACS Applied Materials & Interfaces 15 (2023) 56022–56033.
[34] Q. Zhou, H. Li, C. Du, Z. Ye, L. Liang, G. Chen, High-performance flexible thermoelectric generators with tunable in-plane and out-of-plane architectures, Nano Energy 118 (2023) 109007.

[35] S. Masoumi, E. Nadimi, F. Hossein-Babaei, Electronic properties of Ag-doped ZnO: DFT hybrid functional study, Physical Chemistry Chemical Physics 20 (2018) 14688–14693.
[36] H. Cho, D. Jang, J. Yoon, Y.-S. Ryu, B. Lee, B. Lee, S. Chung, Y. Hong, Milliwatt-scale body-heat harvesting using stretchable thermoelectric generators for fully untethered, self-sustainable wearables, ACS Energy Letters 8 (2023) 2585–2594.
[37] Y. Lu, Y. Zhou, W. Wang, M. Hu, X. Huang, D. Mao, S. Huang, L. Xie, P. Lin, B. Jiang, Staggered-layer-boosted flexible Bi2Te3 films with high thermoelectric performance, Nature Nanotechnology 18 (2023) 1281–1288.
[38] X. Yuan, Z. Li, Y. Shao, D. Yang, K. Hu, H. You, Z. Xu, S. Hua, W. Liu, P. Peng, Bi 2 Te 3-based wearable thermoelectric generator with high power density: from structure design to application, Journal of Materials Chemistry C 10 (2022) 6456–6463.
[39] D.W. Ao, W.D. Liu, Y.X. Chen, M. Wei, B. Jabar, F. Li, X.L. Shi, Z.H. Zheng, G.X. Liang, X.H. Zhang, Novel thermal diffusion temperature engineering leading to high thermoelectric performance in Bi2Te3-based flexible thin-films, Advanced Science 9 (2022) 2103547.
[40] C. Hollar, Z. Lin, M. Kongara, T. Varghese, C. Karthik, J. Schimpf, J. Eixenberger, P.H. Davis, Y. Wu, X. Duan, High-performance flexible bismuth telluride thin film from solution processed colloidal nanoplates, Advanced materials technologies 5 (2020) 2000600.
[41] F. Suarez, D.P. Parekh, C. Ladd, D. Vashaee, M.D. Dickey, M.C. Öztürk, Flexible thermoelectric generator using bulk legs and liquid metal interconnects for wearable electronics, Applied Energy 202 (2017) 736–745.
[42] V. Padmanabhan Ramesh, Y. Sargolzaeiaval, T. Neumann, V. Misra, D. Vashaee, M.D. Dickey, M.C. Ozturk, Flexible thermoelectric generator with liquid metal interconnects and low thermal conductivity silicone filler, npj Flexible Electronics 5 (2021) 5.
[43] Y. Sargolzaeiaval, V. Padmanabhan Ramesh, T.V. Neumann, V. Misra, D. Vashaee, M.D. Dickey, M.C. Öztürk, Flexible thermoelectric generators for body heat harvesting – Enhanced device performance using high thermal conductivity elastomer encapsulation on liquid metal interconnects, Applied Energy 262 (2020) 114370.
[44] S. Yang, Y. Li, L. Deng, S. Tian, Y. Yao, F. Yang, C. Feng, J. Dai, P. Wang, M. Gao, Flexible thermoelectric generator and energy management electronics powered by body heat, Microsystems & Nanoengineering 9 (2023) 106.
[45] D. Mao, J. Yang, M. Han, X. Huang, J. Wang, B. Jia, Z. Wang, X. Xu, L. Xie, Y. Zhou, G. Li, G.W. Ho, J. He, Homo-layer flexible Bi₂Te₃-based films with high thermoelectric performance, Science Advances 11 (2025) eadz1019.
[46] S. Masoumi, S. O'Shaughnessy, A. Pakdel, Organic-based flexible thermoelectric generators: From materials to devices, Nano Energy 92 (2022) 106774.
[47] Y. Zhao, G.-S. Tang, Z.-Z. Yu, J.-S. Qi, The effect of graphite oxide on the thermoelectric properties of polyaniline, Carbon 50 (2012) 3064–3073.
[48] C. Li, H. Ma, Z. Tian, Thermoelectric properties of crystalline and amorphous polypyrrole: A computational study, Applied Thermal Engineering 111 (2017) 1441–1447.
[49] J.L. Blackburn, A.J. Ferguson, C. Cho, J.C. Grunlan, Carbon-Nanotube-Based Thermoelectric Materials and Devices, Advanced Materials 30 (2018) 1704386.
[50] Z. Fan, P. Li, D. Du, J. Ouyang, Significantly Enhanced Thermoelectric Properties of PEDOT:PSS Films through Sequential Post-Treatments with Common Acids and Bases, Advanced Energy Materials 7 (2017) 1602116.
[51] K. Xu, T.-P. Ruoko, M. Shokrani, D. Scheunemann, H. Abdalla, H. Sun, C.-Y. Yang, Y. Puttisong, N.B. Kolhe, J.S.M. Figueroa, J.O. Pedersen, T. Ederth, W.M. Chen, M. Berggren, S.A. Jenekhe, D. Fazzi, M. Kemerink, S. Fabiano, On the Origin of Seebeck Coefficient Inversion in Highly Doped Conducting Polymers, Advanced Functional Materials 32 (2022) 2112276.

[52] M. Massetti, S. Bonfadini, D. Nava, M. Butti, L. Criante, G. Lanzani, L. Qiu, J.C. Hummelen, J. Liu, L.J.A. Koster, M. Caironi, Fully direct written organic micro-thermoelectric generators embedded in a plastic foil, Nano Energy 75 (2020) 104983.
[53] H. Li, Z. Ding, Q. Zhou, J. Chen, Z. Liu, C. Du, L. Liang, G. Chen, Harness high-temperature thermal energy via elastic thermoelectric aerogels, Nano-Micro Letters 16 (2024) 151.
[54] C. Du, M. Cao, G. Li, Y. Hu, Y. Zhang, L. Liang, Z. Liu, G. Chen, Toward Precision Recognition of Complex Hand Motions: Wearable Thermoelectrics by Synergistic 2D Nanostructure Confinement and Controlled Reduction, Advanced Functional Materials 32 (2022) 2206083.
[55] H. Lv, L. Liang, Y. Zhang, L. Deng, Z. Chen, Z. Liu, H. Wang, G. Chen, A flexible spring-shaped architecture with optimized thermal design for wearable thermoelectric energy harvesting, Nano Energy 88 (2021) 106260.
[56] R. Kiflemariam, C.-X. Lin, Numerical simulation and parametric study of heat-driven self-cooling of electronic devices, Journal of Thermal Science and Engineering Applications 7 (2015) 011008.
[57] Y.G. Lee, J. Kim, M.S. Kang, S.H. Baek, S.K. Kim, S.M. Lee, J. Lee, D.B. Hyun, B.K. Ju, S.E. Moon, Design and experimental investigation of thermoelectric generators for wearable applications, Advanced Materials Technologies 2 (2017) 1600292.
[58] Y. Wang, Y. Shi, D. Mei, Z. Chen, Wearable thermoelectric generator for harvesting heat on the curved human wrist, Applied Energy 205 (2017) 710–719.
[59] C.S. Kim, G.S. Lee, H. Choi, Y.J. Kim, H.M. Yang, S.H. Lim, S.-G. Lee, B.J. Cho, Structural design of a flexible thermoelectric power generator for wearable applications, Applied Energy 214 (2018) 131–138.
[60] L.-S. Zhang, B. Yang, S.-P. Lin, T. Hua, X.-M. Tao, Predicting performance of fiber thermoelectric generator arrays in wearable electronic applications, Nano Energy 76 (2020) 105117.
[61] A. Nozariasbmarz, F. Suarez, J.H. Dycus, M.J. Cabral, J.M. LeBeau, M.C. Öztürk, D. Vashaee, Thermoelectric generators for wearable body heat harvesting: Material and device concurrent optimization, Nano Energy 67 (2020) 104265.
[62] S. Fan, Y. Gao, A. Rezania, Thermoelectric performance and stress analysis on wearable thermoelectric generator under bending load, Renewable Energy 173 (2021) 581–595.
[63] A. Zhang, G. Li, B. Wang, J. Wang, A Theoretical Model for Wearable Thermoelectric Generators Considering the Effect of Human Skin, Journal of Electronic Materials 50 (2021)
[64] K. Gürkan, H. Karaman, S. Ballikaya, Optimization of high-performance flexible thermoelectric generator from material synthesis to simulation and device application, Energy Conversion and Management 291 (2023) 117335.
[65] T. Ma, Z. Qu, X. Yu, X. Lu, Y. Chen, Q. Wang, Numerical study and optimization of thermoelectric-hydraulic performance of a novel thermoelectric generator integrated recuperator, Energy 174 (2019) 1176–1187.
[66] S. Masoumi, M. Shokrani, S. Aghili, F. Hossein-Babaei, Zinc oxide-based direct thermoelectric gas sensor for the detection of volatile organic compounds in air, Sensors and Actuators B: Chemical 294 (2019) 245–252.
[67] K. Tang, D. Yang, K. Hu, J. Li, J. Wang, Y. Wu, T. Ming, Y. Yan, Q. Zhang, C. Uher, Multi-factor roadmap for designing wearable micro thermoelectric generators, Energy Conversion and Management 280 (2023) 116819.
[68] F. Suarez, A. Nozariasbmarz, D. Vashaee, M.C. Öztürk, Designing thermoelectric generators for self-powered wearable electronics, Energy & Environmental Science 9 (2016) 2099–2113.

[69] M. Jabri, S. Masoumi, T.R. Kandukuri, L.G. Occhipinti, Flexible thin-film thermoelectric generators for human skin-heat harvesting: A numerical study, Nano Energy 129 (2024) 110001.
[70] S. Masoumi, M. Jabri, A. Pakdel, Investigating thin-film thermoelectric generators: Leg shape, TEG configuration, and contact resistance analysis, Energy Conversion and Management: X 22 (2024) 100597.
[71] Z. Ouyang, D. Li, Modelling of segmented high-performance thermoelectric generators with effects of thermal radiation, electrical and thermal contact resistances, Scientific Reports 6 (2016) 24123.
[72] Y. Cai, P. Jin, X. Wang, C. Chen, H. Fu, J. Huang, F. Deng, Nature-inspired wearable thermoelectric generator for body heat harvesting, Energy (2025) 138899.
[73] S. Qing, S. Ren, S. Tang, Z. Qiao, Dynamic behaviors of ink-based flexible thin-film thermoelectric generator applied for harvesting human body waste heat, Energy 335 (2025) 137926.
[74] S. Ren, S. Qing, S. Tang, E. Peng, Performance limits of wearable ink-based thin-film thermoelectric generator for human-body waste heat recovery, Energy Conversion and Management 300 (2024) 117960.
[75] J. Lv, X. Li, Z. An, Z. Shi, Y. Li, Y. Xu, J. Liu, Q. Liu, A Self-Powered Flexible Bioelectronic System Based on Thermoelectric Generator for Electrotherapy and Monitoring of Chronic Wounds, Advanced Materials Technologies 10 (2025) e00332.
[76] P. Webb, Temperatures of skin, subcutaneous tissue, muscle and core in resting men in cold, comfortable and hot conditions, European Journal of Applied Physiology and Occupational Physiology 64 (1992) 471–476.
[77] D. Enescu, Heat transfer mechanisms and contributions of wearable thermoelectrics to personal thermal management, Energies 17 (2024) 285.